# Pipe flow transition threshold following localized impulsive perturbations

Fernando Mellibovsky[*] and Alvaro Meseguer[†]

*Departament de Física Aplicada, Universitat Politècnica de Catalunya,*

*C/ Jordi Girona 1-3, Mod. B5, 08034 Barcelona, SPAIN*

(Dated: July 19, 2006)

## Abstract

A numerical study of the destabilizing effects of localized impulsive perturbations in pressure-driven Hagen-Poiseuille or pipe flow is presented. The numerics intend to ellucidate the intrinsic mechanisms of subcritical transition to turbulence in pipe flow by reproducing very recent experimental explorations carried out by Hof, Juel and Mullin [1], concluding that the minimum amplitude of a perturbation required to cause transition scales as the inverse of the Reynolds number, i.e., $\mathcal{O}(\mathrm{Re}^{-1})$. The numerical model simulates the experimental disturbance generator based on impulsive injection of fluid through six slits azimuthally equispaced on a perimeter around the pipe. This is accomplished by introducing a local time-dependent impulsive volume force term in the Navier-Stokes equations for the perturbation velocity field, fulfilling incompressibility constraints. A comprehensive exploration of the critical amplitudes that trigger transition as a function of the injection duration is carried out. It is concluded, in agreement with experiments, that injections lasting longer than $\Delta t_{\mathrm{inj}} \simeq 24$ advective time units do not remarkably decrease the critical amplitude of transition. Threshold amplitudes for long enough injections are then computed within the range $\mathrm{Re} \in [2000, 14125]$. For $\mathrm{Re} \gtrsim 4000$ the numerical results agree with the experiments. However, for $\mathrm{Re} \lesssim 2800$, neat transitions are very difficult to obtain, being impossible to provide an accurate value of the critical amplitude. The apparent disagreement with the sound regular slope of the experimental threshold is explained in terms of the differences between constant mass-flux versus pressure-driven pipe flows.

PACS numbers: 47.20.Ft, 47.20.Gv, 47.32.-y, 47.54.+r

---

[*] Electronic mail:fmellibovsky@fa.upc.edu

[†] Corresponding author's e-mail:alvar@fa.upc.edu

## I. INTRODUCTION

Transition to turbulence in Hagen-Poiseuille flow (fluid flow through a pipe) has been object of analysis for over a century. Since Osborne Reynolds published the first study[2] regarding instability phenomena in pipe flows, many theoretical[3–6], numerical[7–13] and experimental[1,14–16] fluid dynamicists have devoted enormous efforts to clarify the inner mechanisms that are responsible for the eventual transition to turbulence of this classical problem of fluid dynamics.

Although there is no formal proof, comprehensive numerical linear stability analyses[7,10,17–19] suggest that Hagen-Poiseuille or pipe flow (HPF) is always stable with respect to infinitesimal perturbations for any value of the Reynolds number (Re). In practice, the flow exhibits natural transition to turbulence in the laboratory for Reynolds numbers above Re $\simeq$ 2000, i.e., a *subcritical* transition[17]. Experimental evidence shows that pipe flow becomes more sensitive to perturbations when increasing Re, but experiments carried out under extremely careful conditions may remain laminar for very high speeds of the fluid. Since the basic flow is linearly stable, finite (but small) amplitude perturbations must be responsible for the transition to turbulence.

During the last decade, the pursuit of an explanation of the instability phenomenon in pipe flow has followed two independent research approaches. The first one has been mainly focused on the study of the effects of nonmodal transient growth exhibited by streamwise vortical finite amplitude perturbations, due to the strong nonnormality of the linearized Navier-Stokes operator, i.e., non-orthogonality of its eigenvectors[7,11,20,21]. The second has focused on the exploration of the phase map of the corresponding dynamical system representing the fluid problem. Numerical studies have recently revealed the existence of travelling waves of selected azimuthal symmetry, presumably constituting the essential topological features of the chaotic dynamics[5,9] observed. The limit cycles associated with these travelling waves have been proved to be linearly unstable and their associated friction factor reasonably agrees with the empirical laws describing turbulent flows in smooth pipes[5], as a clear sign of the relevance of these solutions in the turbulent regime. Postprocessed experimental results have recently suggested the presence of the aforementioned travelling waves as inherent components of the turbulent flow[22].

One of the main goals of the two previously described approaches to subcritical turbulence

in HPF has been to provide a characterization of the *basin of attraction* of this basic laminar solution, i.e., a subset in an infinite dimensional space that contains the basic flow, driving towards it any initial perturbation contained in this subset. Numerical simulations confirm that HPF is even stable for *all* axisymmetric finite-amplitude disturbances[23]. Therefore, the basin of attraction *is not* a bounded set and its *size* is a meaningless measure because it is actually infinite. Instead, we must think of the *critical threshold* as the boundary of that basin of attraction that approaches a minimum norm $A$ from the steady solution. A question still unsolved is the dependence of this norm or amplitude with respect to the Reynolds number, $A = A(\mathrm{Re})$, that must necessarily decrease when Re is increased, being plausible to assume that its asymptotic behaviour scales with Re according to

$$A \sim \mathrm{Re}^{\gamma}, \tag{1}$$

with $\gamma$ necessarily negative. In other words, $A$ represents the minimum amplitude of a perturbation capable of destabilizing the basic profile, thus leading to a turbulent regime.

Expression (1) implicitly involves many physical aspects that require an accurate description. First, a mathematical definition of the amplitude $A$ appearing in (1) must be provided. Second, the geometrical features of the perturbation (azimuthal symmetry or streamwise dependence, for example) will necessarily conditionate the subspace over which we are measuring the amplitude appearing in (1). Third, depending on the perturbative methodology used, the dynamical system scenario of the problem may fall into two different categories. Either the perturbation may develop from an initial disturbance of the basic flow, the fluid system evolving in an *autonomous* fashion, or it may develop from a *time-dependent* source such as an external forcing or time-dependent boundary conditions. Fourth, when studying the time evolution of a perturbation in an open flow, advection is crucial, since potential turbulent transients flush down the drain, making it impossible to classify the dynamics for long times. Once an observational *time-horizon*, say $T$, is chosen, one must establish criteria to distinguish between laminar, relaminarized or turbulent states. As a result, the critical exponent appearing in (1) will implicitly depend on the time horizon chosen[24], i.e., $\gamma = \gamma(T)$. Fifth, expression (1) is only meaningful for high values of Re.

Theoretical exponents for plane channel flows have been obtained by means of asymptotic methods within the framework of some particular transition scenarios[25]. For pipe flow, recent renormalizations[26] have been suggested in order to cast different experimental results

in terms of a single definition of the amplitude appearing in (1), providing lower and upper bounds for the value of this critical exponent that presumably lies within the interval $\gamma \in [-9/5, -6/5]$.

Very recent experiments carried out by Hof, Juel & Mullin[1], henceforth referred as HJM, explored transition phenomena of pipe flow subjected to finite amplitude impulsive perturbations for a wide range of axial speeds of the flow. The experiments reported in HJM were carried out in a long aspect ratio pipe, with a piston that kept the mass-flux constant during every run and where the disturbances were generated by impulsively injecting fluid into the main flow through six slits azimuthally equispaced on a perimeter around the pipe located at a fixed axial position far downstream from the pipe inlet, so that the HPF flow was sufficiently developed. The experimental results of HJM clearly concluded that the minimum amplitude of a perturbation required to trigger transition scaled as the inverse of the Reynolds number, i.e., $A = \mathcal{O}(\text{Re}^{-1})$. The experimental procedure of perturbing the basic flow would correspond to the category of time-dependent (non-autonomous) perturbative methods.

By contrast, numerical simulations[11,13] based on initial streamwise perturbations concluded that the minimum amplitude, defined as the square root of the kinetic energy, required to destabilize the flow, scaled as $A = \mathcal{O}(\text{Re}^{\gamma})$, with $\gamma$ between $-1$ and $-3/2$, depending on the type of initial vortical perturbation chosen. The discrepancy with the experimental results might probably relate to the definition of the perturbation amplitude used in Refs. 11,13, which is not applicable to the type of perturbations used in HJM. Nevertheless, transition in pipe flow strongly depends not only on the amplitude of the initial perturbation, but also on its symmetry features, being globally stable, for instance, with respect to axisymmetric perturbations[23]. The perturbation mechanism used in Refs. 11,13 corresponds to the category of autonomous perturbative methods, since there is no time-dependent forcing of the Navier-Stokes problem.

The main goal of this work is to gain some insight on the internal mechanisms responsible for transition by reproducing numerically the experiments of HJM with an accurate spectral method. The main difference between the present study and HJM experimental work concerns the principle driving the fluid along the pipe. The pressure drop (or streamwise forcing) is held constant throughout each of our computations, letting the massflow vary freely as perturbations develop within the flow. Conversely, the experiments force a pre-

4

scribed massflow by means of a time-dependent forcing that, inflicted upon the fluid by a constant-speed sucking piston, injects or substracts energy into or from the flow.

The paper is structured as follows. The mathematical and numerical formulation of the problem are presented in §II, where special attention is given to the modeling of the injection and to relating the numerical injection amplitude to its experimental counterpart. §III deals with the injection-time dependency of the amplitude threshold, comparing it with experimental data. A typical transitional experiment is analyzed in §IV to demonstrate the effects of localized impulsive injections. In §V, an extensive exploration is undertaken to determine the critical amplitude threshold as a function of the Reynolds number. Finally, the main conclusions drawn from this work are summarized in §VI.

## II.   MATHEMATICAL FORMULATION AND PERTURBATION MODELING

We consider the motion of an incompressible viscous fluid of kinematic viscosity $\nu$ and density $\rho$. The fluid is driven through a circular pipe of radius $a$ and infinite length by a uniform pressure gradient, $\Pi_0$, parallel to the axis of the pipe. The problem is naturally formulated in cylindrical coordinates, the velocity of the fluid being given by its radial ($\hat{\boldsymbol{r}}$), azimuthal ($\hat{\boldsymbol{\theta}}$) and axial ($\hat{\boldsymbol{z}}$) components,

$$\mathbf{v} = u\,\hat{\boldsymbol{r}} + v\,\hat{\boldsymbol{\theta}} + w\,\hat{\boldsymbol{z}} = (u\,,\,v\,,\,w), \tag{2}$$

where $u$, $v$ and $w$ depend on the three spatial coordinates $(r, \theta, z)$ and time $t$. The motion of the fluid is governed by the incompressible Navier-Stokes equations

$$\partial_t \mathbf{v} + (\mathbf{v} \cdot \nabla)\mathbf{v} \;=\; -\nabla p - \frac{\Pi_0}{\rho}\hat{\boldsymbol{z}} + \nu \Delta \mathbf{v} \tag{3}$$

$$\nabla \cdot \mathbf{v} \;=\; 0, \tag{4}$$

where $\mathbf{v}$ is the velocity vector field, satisfying the no-slip boundary condition at the wall,

$$\mathbf{v}_{\text{pipe wall}} = \mathbf{0}, \tag{5}$$

and $p$ is the reduced pressure. A basic steady solution of (3-5) is the so-called *Hagen-Poiseuille flow*,

$$\mathbf{v}_{\mathrm{B}} = (u_{\mathrm{B}}\,,\,v_{\mathrm{B}}\,,\,w_{\mathrm{B}}) = \left(0\,,\,0\,,\,-\frac{\Pi_0 a^2}{4\rho\nu}\left[1 - \left(\frac{r}{a}\right)^2\right]\right), \qquad p_{\mathrm{B}} = \mathrm{C}, \tag{6}$$

5

where C is an arbitrary constant. This basic flow is a parabolic axial velocity profile which only depends on the radial coordinate. The velocity of the fluid attains a maximum value $U_{cl} = -\Pi_0 a^2/4\rho\nu$ at the center-line or axis of the cylinder.

Henceforth, all variables will be rendered dimensionless using $a$ and $U_{cl}$ as space and velocity units, respectively. The axial coordinate $z$ is unbounded since the length of the pipe is infinite. In what follows, it will be assumed that the flow is axially periodic with period $b$. In the dimensionless system, the spatial domain $\mathfrak{D}$ of the problem is

$$\mathfrak{D} = [0,1] \times [0, 2\pi) \times [0, \Lambda) \tag{7}$$

where $\Lambda = b/a$ is the dimensionless length of the pipe, in radii units. In the new variables, the basic flow takes the form

$$\mathbf{v}_B = (u_B, v_B, w_B) = (0\ ,\ 0\ ,\ 1 - r^2). \tag{8}$$

The parameter governing the dynamics of the problem is the *nominal* Reynolds number Re, based on the basic laminar flow corresponding to a given axial pressure gradient,

$$\mathrm{Re} = \frac{a U_{cl}}{\nu} = \frac{-\Pi_0 a^3}{4\rho\nu^2}., \tag{9}$$

whereas the *actual* Reynolds number used in the experiments by HJM is defined as

$$\mathrm{Re}_a = \frac{d\ \overline{U}}{\nu}, \tag{10}$$

where $d = 2a$ is the pipe diameter and

$$\overline{U} = \frac{1}{\pi a^2} \int_0^{2\pi} \int_0^a w\ r\ \mathrm{d}r\ \mathrm{d}\theta \tag{11}$$

is the mean axial instantaneous speed of the flow. Accordingly, the actual Reynolds number $\mathrm{Re}_a$ will be an evolving quantity in the Navier-Stokes equations representing a pressure-driven pipe. Both Reynolds numbers coincide for the laminar Hagen-Poiseuille profile, regardless of the pressure-driven or constant mass-flux nature of the problem. In a constant mass-flux pipe, $\mathrm{Re}_a$ is forced to remain always constant through the action of a time-dependent adapting volume force, whereas in a pressure-driven pipe, it exhibits a considerable drop as turbulence sets in.

The flow velocity can be expressed as a sum of the basic flow plus a solenoidal velocity disturbance field vanishing at the pipe wall

$$\mathbf{v}(r, \theta, z, t) = \mathbf{v}_B(r) + \mathbf{u}(r, \theta, z, t), \quad \nabla \cdot \mathbf{u} = 0, \quad \mathbf{u}(1, \theta, z, t) = \mathbf{0}. \tag{12}$$

6

The same sort of decomposition is considered for the pressure field

$$p(r, \theta, z, t) = p_{\mathrm{B}} + q(r, \theta, z, t). \tag{13}$$

Formal substitution of (12-13) in the Navier-Stokes equations leads to a nonlinear initial-boundary problem for $\mathbf{u}$ and $q$,

$$\partial_t \mathbf{u} = -\nabla q + \frac{1}{\mathrm{Re}} \Delta \mathbf{u} - (\mathbf{v}_{\mathrm{B}} \cdot \nabla)\mathbf{u} - (\mathbf{u} \cdot \nabla)\mathbf{v}_{\mathrm{B}} - (\mathbf{u} \cdot \nabla)\mathbf{u}, \tag{14}$$

$$\nabla \cdot \mathbf{u} = 0, \tag{15}$$

$$\mathbf{u}(1, \theta, z, t) = 0, \tag{16}$$

$$\mathbf{u}(r, \theta + 2\pi n, z, t) = \mathbf{u}(r, \theta, z, t), \tag{17}$$

$$\mathbf{u}(r, \theta, z + l\Lambda, t) = \mathbf{u}(r, \theta, z, t), \tag{18}$$

$$\mathbf{u}(r, \theta, z, 0) = \mathbf{u}_0, \quad \nabla \cdot \mathbf{u}_0 = 0, \tag{19}$$

for $(n, l) \in \mathbb{Z}^2$, $(r, \theta, z) \in \mathfrak{D}$ and $t > 0$. Equation (14) describes the nonlinear space-time evolution of the disturbance velocity field. Equation (15) is the solenoidal condition for $\mathbf{u}$, and equations (16)–(18) describe the homogeneous boundary condition for the radial coordinate and the periodic boundary conditions for the azimuthal and axial coordinates, respectively. Finally, equation (19) is the initial solenoidal condition at $t = 0$.

The system (14-19) is spatially discretized by means of a solenoidal spectral Petrov-Galerkin scheme in primitive variables, for which the pressure term $-\nabla q$ cancels out in the projection. The resulting dynamical system of amplitudes is numerically integrated in time by means of a 4th order linearly implicit Backward-Differences method with standard 4th order extrapolation of the non-linear term. In our explorations, the pipe length has been fixed to $\Lambda = 12.8\pi \sim 40$ radii units and the spatial resolution used in the domain $\mathfrak{D}$ has been set to $M_r \times N_\theta \times L_z = 33 \times 65 \times 65$ (radial×azimuthal×axial) grid points, resulting in a dynamical system of nearly $1.4 \times 10^5$ degrees of freedom. No substantial differences have been observed when increasing the resolution. The numerical reliability of the method has been extensively tested for low and high resolution computations[11,27–29].

## A. Numerical model of the six-jet impulsive injection

Equations (14-19) describe the spatio-temporal evolution of an arbitrary perturbation, the source of disturbances being prescribed by the initial condition $\mathbf{u}_0$ in (19). As mentioned

in the Introduction, different scenarios of transition have been studied[11,29] based on specific initial perturbations. In the present work, no initial perturbation is to be prescribed, *i.e.*, $\mathbf{u}_0 = 0$, and the disturbances will be generated by the action of an external forcing.

Figure 1a is a schematic plot of the injection device used in HJM, where the six slits are equally distributed along the perimeter of the pipe so that the injected fluid jet penetrates into the basic flow with an angle $\varphi = \pi/3$ with respect to the radial coordinate, in a plane normal to the pipe axis. In addition, the injection is located at a particular streamwise coordinate for which the basic Hagen-Poiseuille flow profile can be considered as fully developed. Besides, the injection is activated following a step-like time-dependent function, active for a prescribed injection duration. We refer the reader to HJM[1,15] for further details.

Numerical spectral modeling of the device shown in Fig. 1a is not a trivial task. To start with, fluid is injected from the wall, thus violating the homogenous boundary condition (16). Second, we do not know a priori the nature of the injected flow regarding its spatial structure, i.e., laminar or turbulent profile and penetration capability. Third, the boundary condition at the wall is time-dependent, in contrast with (16). Moreover, since the fluid is injected impulsively, which requires a time lapse to do so, the initial condition (19) cannot represent by any means such mechanism.

The aforementioned difficulties can be mostly overcome by means of adding an impulsive volume force term $\mathbf{f}$ in equation (14), playing the role of the injection. This forcing acts locally in time and space as an accelerator of the fluid and can be chosen and suitably modified until the dynamics observed are in agreement with the experimental observations. In this work, we are going to study the perturbative effects generated by introducing in (14) an impulsive volume forcing term, $\mathbf{f}$, localized in time and space, i.e.,

$$\partial_t \mathbf{u} = -\nabla q + \mathbf{f} + \frac{1}{\text{Re}}\Delta \mathbf{u} - (\mathbf{v}_\text{B} \cdot \nabla)\mathbf{u} - (\mathbf{u} \cdot \nabla)\mathbf{v}_\text{B} - (\mathbf{u} \cdot \nabla)\mathbf{u}. \tag{20}$$

The length scale of the experimental injection holes is far too small to be captured in a feasible discretization. As a result, the approach of modeling the effects of an injection, rather than the injection itself, seems a reasonable option. Thus, it is assumed that the only, or of outmost importance, effect of the injection is that of accelerating the fluid around the jet. The forcing field $\mathbf{f}$ appearing in (20) is introduced so that the resulting local acceleration is qualitatively equivalent to the one generated by the injection experimental device. We can properly represent the number of injection points (six) and the angle at

8

which the jets penetrate the pipe ($\pi/3$). The width of the jets in the cross-sectional plane can be more or less approximated, but not so much so in the streamwise direction where a smoother profile must be used due to the *coarse* axial discretization of the domain. Finally, the penetration of the jet becomes the least guided decision to be taken, as no data on this is readily available.

In the present study, the forcing field has the following structure:

$$\mathbf{f}(r, \theta, z, t) = \mathrm{f_a}\, \mathrm{f}_t(t)\, \mathbf{f}_s(r, \theta, z), \tag{21}$$

where $\mathrm{f_a}$ is the amplitude factor. The injection time-dependence is introduced through a double-step function $\mathrm{f}_t(t)$, given by

$$\mathrm{f}_t(t) = \begin{cases} 1 & t \le \Delta t_{\mathrm{inj}} \\ 0 & t > \Delta t_{\mathrm{inj}}, \end{cases} \tag{22}$$

acting as a switch that remains activated within the time interval $t \in [0, \Delta t_{\mathrm{inj}}]$. Finally, $\mathbf{f}_s$ provides the spatial structure of the six-jet injection and its explicit mathematical expression can be found in the Appendix. Figure 1b shows the acceleration field inflicted by the modelled forcing upon the stationary basic flow.

Values of the injection lapse within the range $\Delta t_{\mathrm{inj}} \in [2, 24]$ advective time units have been used throughout the present study. It would make no sense to report on the amplitude factor ($\mathrm{f_a}$) range explored, since it is only intended to scale/modulate the arbitrary original norm of the spatial structure $\mathbf{f}_s$ and therefore has a purely relative meaning.

## B.    Relating the numerical injection amplitude to its experimental counterpart

One of the main difficulties is the quantitative comparison of the effect produced by the numerical injection just formulated and the actual experimental one. Some insight may be obtained from the *axisymmetric jet-theory*[30]. Assuming the jet penetrates a resting fluid in a direction normal to the wall from which it emanates, and that it is locally axisymmetric around its propagation axis, which are rough idealizations, its *kinematic momentum*[30] is

$$\mathrm{K}' = 2\pi \int_0^\infty u(\varrho)^2 \, \varrho \, \mathrm{d}\varrho, \tag{23}$$

where $u(\varrho)$ refers to the jet-wise component of the induced velocity field at a distance $\varrho$ from its axis. The value of $u = u(0)$ on the jet axis, at a distance $g$ from the slit is also provided

by the theory[30],

$$u = \frac{3}{8\pi} \frac{\mathrm{K}'}{\nu g}. \tag{24}$$

The objective is to relate the velocity at a given point on the jet axis to the injected massflow, on which quantity rests the amplitude definition used in the experiments by HJM. In practice, the point where the forcing field $\mathbf{f}$ attains its maximum norm is chosen and the time evolution of the jetwise-projected flow velocity at this point, induced by sustained action of the forcing for all $t$, monitored. Under the assumption that the asymptotic laminar velocity to which the fluid flow tends corresponds to that of an idealized jet, the axisymmetric jet theory can be used to recover the amplitude of the injection that would potentially produce this asymptotic velocity at the particularly chosen point.

The kinematic momentum defined in (23), which must be conserved in the jet axial direction, can be expressed as a function of the injected massflow through one of the slits,

$$\mathrm{K}' = \beta \frac{\Phi_{\mathrm{inj}}^2}{\mathrm{S}_{\mathrm{inj}}}, \tag{25}$$

where $\mathrm{S}_{\mathrm{inj}}$ is the cross-sectional area of the slit and $\beta$ is a parameter depending on the jet velocity profile considered ($\beta = 4/3$ or $1$ for a laminar or a turbulent jet, respectively). It will be assumed that the penetrating jet will commonly be turbulent. By identifying our *finite-area* and *finite-velocity* jet with a *zero-area* and *infinite-velocity* ideal jet, both carrying the same kinematic momentum, the center-line velocity of the jet at a distance $g$ from the slit, where our forcing is maximum, is

$$u = \frac{3}{8\pi\nu g} \frac{\Phi_{inj}^2}{\mathrm{S}_{\mathrm{inj}}}. \tag{26}$$

The *injection amplitude* $\mathcal{A}$ defined in HJM is given by the ratio between the total massflow injected through the $N_{\mathrm{inj}}$ slits and the pipe massflow upon injection,

$$\mathcal{A} = N_{\mathrm{inj}} \frac{\Phi_{\mathrm{inj}}}{\Phi_{\mathrm{pipe}}}. \tag{27}$$

The pipe massflow can be exactly derived from the actual Reynolds number, $\mathrm{Re}_a$, in the experiments, or, equivalently, from the nominal Reynolds number before injection. In our computations, the pipe massflow evolves, but, provided that the injection duration is kept short, it can be considered that of the initially unperturbed Hagen-Poiseuille flow, so that it can be expressed in terms of the nominal Reynolds number, Re, as

$$\Phi_{\mathrm{pipe}} = \frac{\pi\nu a}{2} \mathrm{Re}. \tag{28}$$

Using equations (26) and (28), the injection amplitude defined in (27) can be expressed in terms of the speed of the jet and the nominal Reynolds number,

$$\mathcal{A} = N_{\mathrm{inj}} \left( \frac{32}{3} g^* \mathrm{S}^*_{\mathrm{inj}} \right)^{1/2} \left( \frac{u^*}{\mathrm{Re}} \right)^{1/2}, \tag{29}$$

where $g^* = g/a$, $\mathrm{S}^*_{\mathrm{inj}} = \mathrm{S}_{\mathrm{inj}}/\pi a^2$ and $u^* = u/\mathrm{U}_{\mathrm{cl}}$ are dimensionless quantities measuring the distance from the slit, its cross-sectional area and the jet speed, respectively. It should be reminded that $u^*$ appearing in (29) *is not* the velocity of the flow at the chosen point projected on the jet axis direction (which we shall call $u_g$), but the velocity at that point of the jet itself, the effects of which we are trying to model using a forcing field. While we have access to the former, we infer the latter by assuming that they become the same as the effects of the forcing saturate and the velocity at this point approaches an asymptotic value.

Different jet-penetration scenarios have been suggested[26] recently in order to adjust upper and lower bounds for the threshold exponent $\gamma$ appearing in (1). To the authors' knowledge, equation (29) provides a first quantitative approximation to a law relating an injection property that is mensurable in under-resolved (to be affordable) computations and the experimental amplitude. There are other factors appearing in (29) that are associated with geometrical features of the slit. As mentioned before, current computational power limitations makes accurate representation of the slits not feasible. As a result, the *coarse* discretization used in this study may lead to discrepancies due to geometrical differences between the numerically modelled and the actual experimental injections. Nevertheless, we expect to qualitatively mimic the experimental behaviour of the injection save for a scaling factor to do with geometrical discrepancies and non-ideality of the jets.

## III.   EFFECTS ON TRANSITION OF INJECTION DURATION

The effect of the injection lapse on transition has been extensively tested experimentally in HJM and it has been found that, although increasing the duration of the injection at a given Reynolds number reduces the critical amplitude, this reduction eventually stagnates. As a result, the critical amplitude does not depend on the injection duration, provided that it becomes sufficiently long-lasting. Experimentally, it has been observed that the critical amplitude is not altered for injection durations of $\Delta t_{\mathrm{inj}} \gtrsim \Delta t_0 = 24$ advective time units, where $\Delta t_0$ will be considered later as a reference time interval for amplitude renormalization

11

purposes. This behaviour should also be reproduced numerically for the simulations to be considered reliable.

Following HJM, we proceed to validate the computational model of the injection and the scaling law provided in (29) by simulating different injection amplitudes and injection lapses at Re = 4000. For a given injection lapse, $\Delta t_{\mathrm{inj}}$, the amplitude factor $f_a$ is increased until transition is obtained. A computational run is considered turbulent when chaotic dynamics have taken over the full domain and persist after 600 advective time units. Laminar runs, instead, are characterized by the eventual viscous decay of the injected perturbation after an initial transient growth.

Once the critical forcing amplitude is known, we proceed to compute the asymptotic value $u^*$ of the jet by re-starting the same critical run but with the forcing permanently on so that the flow jetwise speed at the chosen location on the jet axis, $u_g(t)$, has enough time to stagnate to its asymptotic value, which we identify as $u^*$. This recomputation is mandatory for example in the case of very short injections, where the forcing stops before the monitored flow speed has achieved an asymptotic value.

Figure 2a shows the flow speed $u_g(t)$ measured at the point of maximum forcing norm for different critical runs carried out for $\Delta t_{\mathrm{inj}} = 2, 3, 4, 5, 8$ and 16 time units. On each of these curves the forcing was stopped at the indicated instants of time (gray circles), critically leading to transition for longer times (not shown). Figure 2a also shows the behaviour of the flow speed for the same runs, but with permanent forcing (dashed curves). It can be observed that there is a clear stagnation of $u_g$ to a constant value $u^*$ in some cases. The curve for $\Delta t_{\mathrm{inj}} = 2$ exhibits some irregularities due to the fact that very large amplitudes are needed to lead to transition for short injections and therefore turbulence sets in before the asymptotic value of the jet speed is reached. However it is easy to obtain a sharp asymptotic value $u^*$ for most of the injections, so that this value can be used afterwards in relation (29) to identify its corresponding amplitude $\mathcal{A}$.

In order to make a consistent comparison between numerics and experiments, we define the *normalized amplitude* of a $\Delta t_{\mathrm{inj}}$-lapse perturbation as

$$\mathrm{A}(\Delta t_{\mathrm{inj}}) = \frac{\mathcal{A}(\Delta t_{\mathrm{inj}})}{\mathcal{A}(\Delta t_0)}. \tag{30}$$

Therefore, the experimental and numerical threshold amplitudes are normalized *independently* with respect to their corresponding reference saturation values for $\Delta t_0 = 24$ advec-

tive time units. With this renormalization, the critical amplitudes become independent of the injection geometrical features appearing in (29) and comparison is rendered possible. Table I summarizes the saturation values $u^*$ obtained from the computations and their corresponding amplitudes according to (29) and (30), $\mathcal{A}_{\mathrm{num}}$ and $\mathrm{A}_{\mathrm{num}}$, respectively. Table I also contains the experimental data, $\mathcal{A}_{\mathrm{exp}}$, originally extracted from Figure 3 of HJM[1] and normalized, $\mathrm{A}_{\mathrm{exp}}$, according to (30). Figure 2b shows the normalized threshold amplitudes $\mathrm{A}_{\mathrm{exp}}$ and $\mathrm{A}_{\mathrm{num}}$ for different injection lapses. The agreement is very good, particularly for $\Delta t_{\mathrm{inj}} > 8$. Nevertheless, there is some discrepancy for short injections, $\Delta t_{\mathrm{inj}} = 2$. As explained before, short injections require a larger forcing, thus triggering transition before an asymptotic value of $u^*$ is identified (see Fig. 2a) to be used in the renormalization. Furthermore, the forcing field has not been tuned to accomodate the large penetration expected from the large amplitude injections required to trigger transition for low $\Delta t_{\mathrm{inj}}$.

The same sort of analysis was carried out in HJM for Re $= 2170$, obtaining equivalent results regarding the stagnation of $\mathcal{A}_{\mathrm{exp}}$ for long injection lapses. The experiment at this lower Re could not be reproduced numerically as it was found very difficult to obtain sustained transition below Re $= 2800$. Sustained turbulence appeared extremely sensitive to environmental noise at the low Re-range, in agreement with what was already pointed out by Reynolds[2] in the past. This was ascertained by increasing the numerical noise at random for different runs, which eased transition but still thwarted any possibility of repeating the injection-lapse analysis at low Re. The incapability of the numerical model to reproduce sustained turbulent motion at Re $\lesssim 2800$ can be ascribed to the pressure-driven nature of the problem, an issue that will be addressed later on.

## IV. TRANSITION DUE TO A LOCALIZED IMPULSIVE INJECTION

The transition process triggered by a localized impulsive injection will be exemplified with a thorough analysis of a single critical run at Re $= 4000$. A very structured and regular disturbance is locally enforced during an injection lapse of $\Delta t_{\mathrm{inj}} = 20$ advective time units. The perturbed portion of fluid at injection withdrawal will nevertheless be much shorter than $\Delta t_{\mathrm{inj}}$-radii, and, tipically, even shorter than $\Lambda/4$. Even though the injection lasts long, only the near-wall region is affected by a forcing representing very oblique jets. In this region, the streamwise advection due to the basic flow is slow and, therefore, the perturbed

13

length remains short. This is clearly shown in Fig. 3a, where the azimuthal vorticity of the disturbance velocity, $(\nabla \times \mathbf{u})_\theta$, is plotted precisely at the end of the injection lapse $t = \Delta t_{\text{inj}} = 20$. Also plotted is a 3D view of a couple of axial vorticity iso-surfaces at $(\nabla \times \mathbf{u})_z = \pm 0.3$, which give a clearer view of the size of the perturbed patch as well as of its laminar or turbulent nature.

Once the injection has ceased, the perturbed patch of flow stretches and deforms as it is advected downstream. The patch follows a cyclic evolution by which it grows and then splits in three sections: front, central and rear. The front and rear sections of the perturbed region travel faster and slower than the central section, respectively, as they die away. Meanwhile, the central region starts stretching again and the whole cycle is repeated. As a result, the length of the perturbed region can be considered to oscillate around a fairly constant value, albeit only transiently while laminarity is preserved. Fig. 3b shows the perturbation immediately after it first breaks into three smaller patches. In Fig. 3c, the front and rear sections of the patch can be seen fading out as they depart from the central section position. What brings this cyclic behavior to an end is the appearance of turbulent motion within the perturbed region. The patch starts losing its laminarity and breaks into turbulent bursts. At first, the turbulent bursts relaminarize at the front and back of the perturbed structure, but soon the core of the perturbed region becomes turbulent and starts growing monotonically. Fig. 3d, shows the perturbation once it has become fully turbulent and is growing fast. From this point on, the trailing edge starts to abruptly decelerate while the leading edge accelerates, rapidly polluting the whole computational domain through axial periodicity reinfection. In experiments, the whole pipe would have transitioned downstream from the axial location where the trailing edge finally settles.

The local growth of the trailing and leading interfaces of the turbulent patch have been monitored during the last stages of the transition, before the turbulent structure pollutes the whole computational domain due to the artificially imposed axial periodic boundary conditions. The root-mean-square (r.m.s.) of the fluctuation of the axial velocity disturbance, $\langle u_z \rangle_{\text{rms}}$, has been computed by taking an average over the azimuthal coordinate, and then further averaged along the radius to produce a quantity representative of the turbulence level and only depending on the axial coordinate. In Fig. 4, the axial positions with $\langle u_z \rangle_{\text{rms}}^2 \geq 0.5\%(\text{U}_{\text{cl}}/2)^2$ have been represented with black dots for $t \in [175, 205]$, evidencing the turbulent patch length evolution as a function of time. Linear regression analyses have

been performed with the first and last point defining the leading (LE) and trailing (TE) edges of the perturbation, respectively. The results have been plotted in Fig. 4 as dashed lines. The slope of these lines represents the propagation velocity of the leading and trailing edges, which happen to be $c_{LE} = 0.754U_{cl}$ and $c_{TE} = 0.325U_{cl}$, respectively. Taking into account that $Re_a \simeq 3850$ during the period we measure these speeds we can express them in terms of the mean flow velocity as $c_{LE} = 1.567\bar{U}$ and $c_{TE} = 0.675\bar{U}$, which is in reasonable agreement with experimental results for turbulent slugs[14]. We can therefore conclude that the numerically observed turbulent structure closely resembles a *slug*. Beyond the times plotted, the leading edge velocity sharply increases, but this is probably due to the fact that the actual size of the perturbed region is comparable to the size of the pipe and the leading and trailing interfaces artificially interact due to the periodic boundary conditions, the infinite pipe no longer being properly represented.

Overall, the transition process which takes the flow from the laminar to the turbulent state is clearly catastrophic, in agreement with what is generally observed in the experiments[15]. Therefore, it is not a trivial task to identify a simple instability mechanism from the numerical computations, in contrast with former numerical studies[13] based on particular streamwise transition scenarios.

## V.   CRITICAL AMPLITUDE THRESHOLD FOR INJECTED PERTURBATIONS

It has been experimentally shown[1] and computationally verified in §III that the critical amplitude of an injection triggering transition does not depend on the injection duration for $\Delta t_{inj} \geq 24$ advective time units. Nonetheless, it can be considered to have reasonably settled down for $\Delta t_{inj} \geq 20$. It is therefore convenient to explore the critical amplitude threshold using this lower $\Delta t_{inj} = 20$, so that the perturbed length is as much shorter than the pipe length as possible to avoid reinfection due to axial periodicity, at least within the injection lifetime.

The critical amplitude threshold has been systematically tracked for Reynolds numbers in the range $Re \in [2512, 14125]$ and the injection duration held fixed to $\Delta t_{inj} = 20$ in all the explorations. The amplitude calculation is completely analogous to the one described in §III and the same criteria used to distinguish laminar from turbulent runs are retained. The geometrical discrepancies between experiments and the actually modelled injection, along

15

with the extreme idealization of the jets, demand a normalization of the experimental and numerical thresholds so that they become comparable. In what follows, we normalize the amplitudes according to

$$A(\text{Re}) = \frac{\mathcal{A}(\text{Re})}{\mathcal{A}(\text{Re}_0)}. \tag{31}$$

where Re is the Reynolds number (actual and nominal confounded) of the basic flow before being perturbed and $\text{Re}_0 = 14000$.

The critical amplitude threshold results are shown in Fig. 5. The amplitude A, normalized according to (31), has been plotted as a function of Re for both experiments (gray squares) and computations (white circles), along with a dashed line indicating a slope of $\gamma = -1$. It is remarkable how experiments and computations exhibit very similar behaviour at high Re, which seems to evidence that the numerical model properly captures the transition mechanisms observed in the laboratory. At the low Re-range, however, while experiments exhibit the same characteristic asymptotic behaviour from Re values as low as 2000, the computations fail to do so. In fact, the numerical simulations seem to find a vertical stability threshold for $\text{Re} \sim 2500$, at least for the type of perturbations used. This discrepancy can be ascribed to several apparent differences between experiments and computations.

A first difference has to do with the topological modelization of the injection. As Re is reduced, the critical amplitude of the forcing required to trigger transition increases. For consistency, the computational forcing field modeling the injection has been held fixed and merely scaled up until transition is obtained. However, in the laboratory, increasing the injection amplitude not only scales up the induced acceleration field, but it also may modify the topological features of the resulting jet, such as its penetration or effective width. The forcing field chosen seems to be as effective as the experimental one for moderate and large Re, but not so much so for low Re. However, we believe this could explain a slight deviation, but not the spectacular discrepancy observed at very low Re.

The main difference, however, concerns the constant-massflow and pressure-driven different nature of the experimental and the computational pipes, respectively. As the perturbation grows and reorganizes the flow, the actual Reynolds $\text{Re}_a$ has a tendency to drop. Especially in short pipes, where intermittency phenomena may fill a high portion of the pipe length. In the constant-massflow experiments of HJM, some energy may be restituted into the flow through the action of a constant-speed piston, so that $\text{Re}_a$ is held constant. In

16

the extreme case of transition, the piston is forced to pull harder in order to restitute the enormous amount of energy dissipated due to turbulence and keep the massflow constant. By contrast, the numerical simulation lets $Re_a$ evolve freely. As a consequence, by the time the perturbation has grown and transition becomes probable, $Re_a$ may be much lower than originally, rendering the experimentally calculated critical amplitude threshold not generally applicable to our simulations, since it is not immediately apparent which value of $Re_a$ (initial, transitional or averaged) should be used for a consistent comparison. This difficulty in choosing when to measure $Re_a$ is in fact disclosing a more profound hindrance, namely that the discrepancy stems from the fact that the problems being solved are indeed different. Fortunately, this effect, which is dominant at low Re for the pipe length considered, becomes less decisive as Re is increased, which indicates that both problems tend to become equivalent. This is clearly evidenced in Fig. 6, where the transient drop of $Re_a$ relative to its initial value, the nominal Re, is followed in time for injection amplitudes that are just subcritical. It is clear that $Re_a$ suffers a transient remarkable drop for low-Re runs (over a 20% at Re = 2818), while at high Re it remains much more stable (less than 2% drop at Re = 14125). The significant drop makes it futile to reproduce the critical amplitude threshold behaviour at low Re, while comparison with experiments becomes reasonable as Re is increased.

## VI. CONCLUSIONS

The effects of the impulsive perturbative system recurrently used in pipe flow experiments have been succesfully modelled via a time-dependent volume forcing in numerical computations. The axisymmetric jet theory has been used to define a perturbation amplitude equivalent to the one used in the aforementioned experiments.

An extensive study of the critical amplitude of the impulsive injections that are capable of triggering transition as a function of their time-duration has been carried out at Re = 4000 and very good agreement with experimental results has been obtained. As in the experiments, the critical amplitude has been shown to decrease with the injection duration to end up stagnating at a constant value for $\Delta t_{\mathrm{inj}} \geq 24$ advective time units.

The evolution of injected perturbations has been monitored with detail in order to capture the main features of a turbulent patch for Re = 4000. Numerical computations reproduce

17

quite well the generation of laminar-turbulent intermittency dynamics observed in former experimental studies. This is evidenced by monitoring the speed of the trailing and leading interfaces of the generated turbulent slug, which are found to be roughly the same as the ones measured in the laboratory. However, the length of the computational pipe domain and the assumption of periodic boundary conditions makes it impossible to study the evolution of the slug for longer times, due to the numerical interaction between the trailing and leading interfaces.

The critical amplitude threshold has been systematically tracked for Reynolds numbers within the range $\text{Re} \in [2512, 14125]$. The explorations have been carried out always taking $\Delta t_{\text{inj}} = 20$, for which the critical amplitude can be considered to have almost settled down to its asymptotic value. Very good agreement with experiments has been obtained at the high-end of Reynolds numbers, where the exponential scaling $A \sim \text{Re}^{-1}$ has been clearly evidenced. By contrast, the apparent discrepancy at low Reynolds numbers is ascribed to the different behaviour of pressure-driven and constant-massflow pipes of finite length and also to the nature of the injection numerical model, whose topological structure has been held fixed in all simulations. In addition, the massflow transient drop as the perturbation develops within the flow at low Re may explain why the computational pressure-driven pipe seems more robust to perturbations and does not exhibit transition for $\text{Re} \lesssim 2800$. However, this transient drop is shown to lose transcendency as the Reynolds number is increased, thus favoring a better asymptotic agreement between our moderate-length pressure-driven computational pipe and the long constant-massflow experimental pipe.

**Acknowledgments**

## APPENDIX A: SPATIAL STRUCTURE OF THE 6-JET INJECTION MODEL

To construct the spatial structure $\mathbf{f}_s$ of the forcing field $\mathbf{f}$ introduced in (20), a draft skeleton for the acceleration field $\mathbf{a}$ must be generated, observing the main properties that are desired. The consistency of this field in terms of solenoidality and boundary conditions can be initially overlooked, as it will be resolved upon projection onto the Petrov-Galerkin projection basis functions inherited from the numerical method used in the spatial discretization[11,28].

The skeleton for the spatial structure of the forcing term $\mathbf{f}_s$ appearing in (21) is written as a superposition of as many fields as injection points,

$$\mathbf{a}(r, \theta, z) = \sum_{j=0}^{5} \mathbf{a}_j(r, \theta, z) = \sum_{j=0}^{5} \mathbf{a}_0(r, \theta - \frac{\pi}{3} j, z). \tag{A1}$$

Due to the periodic azimuthal distribution of the holes, all of them at the same axial position, only the forcing field frame for the first slit, $\mathbf{a}_0$, needs to be engineered, the rest resulting from simple rotations.

The acceleration field $\mathbf{a}_0$ is set up as an homogeneous field of vectors pointing in the direction of the injection (at an angle $\varphi_0$ with respect to the radial direction), with their magnitude modulated with independent gaussian distributions in the three natural directions: jet-wise, jet-transverse and pipe-streamwise, represented in Fig. 7 by $\hat{\mathbf{x}}_0$, $\hat{\mathbf{y}}_0$ and their vector product $\hat{\mathbf{x}}_0 \wedge \hat{\mathbf{y}}_0$, respectively. Because the acceleration on the walls will have to cancel out, the centre ($i$) for the gaussian distributions, where the acceleration is going to be at its maximum, is drifted along the jet axis a certain distance $g$ within the fluid domain, so that the vector field to be projected does not severely violate the boundary conditions. This helps to avoid great distortion of the prescribed vector field upon obtention of the actual forcing to be used, since we are departing from a field which is closer to an acceptable solution.

This vector field is most easily written in the system of cross-sectional cartesian coordinates $(x, y) = x\,\hat{\mathbf{x}}_0 + y\,\hat{\mathbf{y}}_0$, with origin at ($i$), depicted in Fig. 7. In this coordinate system, the vector field takes its simplest form:

$$\mathbf{a}_0(x, y, z) = (a_x, a_y) = e^{-Ax^2 - By^2 - C\sin^2(\frac{2\pi}{\Lambda} z)} \, \hat{\mathbf{x}}_0, \tag{A2}$$

where $B$ and $C$ govern the jet-transverse and pipe-streamwise widths of the jet, $A$ its jet-wise penetration within the fluid domain and $\Lambda$ is the pipe aspect ratio. Typical values used

throughout the present work have been $A = 15$, $B = 150$, $C = 75$, $\Lambda = 12.8\pi$, $\varphi_0 = \pi/3$ and $g = 0.25$.

The local $(x, y)$ coordinates are related to the polar system $(r, \theta)$ according to the change

$$
\begin{cases}
x = -(r \cos\theta - r_i \cos\theta_i) \cos(\varphi_i + \theta_i) - (r \sin\theta - r_i \sin\theta_i) \sin(\varphi_i + \theta_i) \\
y = (r \cos\theta - r_i \cos\theta_i) \sin(\varphi_i + \theta_i) - (r \sin\theta - r_i \sin\theta_i) \cos(\varphi_i + \theta_i),
\end{cases}
\tag{A3}
$$

where $(r_i, \theta_i)$ and $\varphi_i$ are the polar coordinates of the origin of the cartesian coordinate system and its orientation, respectively. Note that in Fig. 7, $\theta_i$ is negative. These quantities follow directly from the injection parameters:

$$
\begin{cases}
r_i = \sqrt{1 + g^2 - 2g \cos\varphi_0} \\
\theta_i = \varphi_0 - \varphi_i \\
r_i \sin\varphi_i = \sin\varphi_0.
\end{cases}
\tag{A4}
$$

The frame of the acceleration field is finally expressed in cylindrical coordinates:

$$
\mathbf{a}_0 = (\mathbf{a}_0)_r \, \hat{\boldsymbol{r}} + (\mathbf{a}_0)_\theta \, \hat{\boldsymbol{\theta}} + (\mathbf{a}_0)_w \, \hat{\boldsymbol{z}} = -a_x \cos(\varphi_i + \theta_i - \theta) \, \hat{\boldsymbol{r}} - a_x \sin(\varphi_i + \theta_i - \theta) \, \hat{\boldsymbol{\theta}}. \tag{A5}
$$

The forcing field skeleton we have just constructed does neither respect the boundary conditions nor the solenoidality condition. A compatible forcing field, $\mathbf{f}_s$, fit to be used in (21), is obtained upon projection of $\mathbf{a}$ in (A1) onto the dual basis of the solenoidal spectral scheme used in this work's spatial discretization[11,28].

---

[1] B. Hof, A. Juel, and T. Mullin, "Scaling of the turbulence transition threshold in a pipe," Phys. Rev. Lett. **91(24),** 244502–4 (2003).

[2] O. Reynolds, "An experimental investigation of the circumstances which determine whether the motion of water shall be direct or sinuous, and of the law of resistance in parallel channels," Phil. Trans. Roy. Soc. Lond. A **174,** 935–982 (1883).

[3] L. Boberg and U. Brosa, "Onset of Turbulence in a Pipe," Z. Naturforsch. **43a,** 697–726 (1988).

[4] U. Brosa and S. Grossmann, "Minimum description of the onset of pipe turbulence," Eur. Phys. J. B. **9,** 343–354 (1999).

[5] H. Faisst and B. Eckhardt, "Travelling waves in pipe flow," Phys. Rev. Lett. **91,** 224502 (2003).

[6] H. Faisst and B. Eckhardt, "Sensitive dependence on initial conditions in transition to turbulence in pipe flow," J. Fluid Mech. **504,** 343–352 (2004).

[7] P. J. Schmid and D. S. Henningson, "Optimal energy growth in Hagen-Poiseuille flow," J. Fluid Mech. **277,** 197–225 (1994).

[8] O. Y. Zikanov, "On the instability of pipe Poiseuille flow," Phys. Fluids **8(11),** 2923–2932 (1996).

[9] H. Wedin and R. R. Kerswell, "Exact coherent structures in pipe flow: travelling wave solutions," J. Fluid Mech. **508,** 333–371 (2004).

[10] A. Meseguer and L. N. Trefethen, "Linearized pipe flow to Reynolds number $10^7$," J. Comput. Phys. **186,** 178–197 (2003).

[11] A. Meseguer, "Streak breakdown instability in pipe Poiseuille flow," Phys. Fluids **15(5),** 1203–1213 (2003).

[12] M. I. Gavarini, A. Bottaro, and F. T. M. Nieuwstadt, "Laminar-turbulent transition in pipe flow for Newtonian and non-Newtonian fluids," J. Fluid Mech. **517,** 131–165 (2004).

[13] F. Mellibovsky and A. Meseguer, "The role of streamwise perturbations in pipe flow transition," Phys. Fluids **18,** 074104 (2006).

[14] I. J. Wygnanski and F. H. Champagne, "On transition in a pipe. Part I. The origin of puffs and slugs and the flow in a turbulent slug," J. Fluid Mech. **59,** 281 (1973).

[15] A. Darbyshire and T. Mullin, "Transition to turbulence in constant-mass-flux pipe flow," J. Fluid Mech. **289,** 83–114 (1995).

[16] A. A. Draad, G. D. C. Kuiken, and F. T. M. Nieuwstadt, "Laminar-turbulent transition in pipe flow for Newtonian and non-Newtonian fluids," J. Fluid Mech. **377,** 267–312 (1998).

[17] P. G. Drazin, *Introduction to Hydrodynamic Stability, Cambridge Texts in Applied Mathematics* (Cambridge Univ. Press, 2002).

[18] A. Leonard and A. Wray, "A new numerical method for the simulation of three–dimensional flow in a pipe," In , E. Krause, ed., Proc. 8th Int. Conf. Num. Meth. Fluid Dyn. (Springer-Verlag, 1982).

[19] V. Priymak and T. Miyazaki, "Accurate Navier-Stokes Investigation of Transitional and Turbulent Flows in a Circular Pipe," J. Comput. Phys. **142,** 370–411 (1998).

[20] P. J. Schmid and D. S. Henningson, "On the role of linear mechanisms in transition to turbulence," Phys. Fluids **6,** 1396–1398 (1994).

[21] M. T. Landahl, "A note on an algebraic instability of inviscid parallel shear flows," J. Fluid Mech. **98,** 243 (1980).

[22] D. Hof, C. W. H. van Doorne, J. Westerweel, F. T. M. Nieuwstadt, H. Faisst, B. Eckhardt, H. Wedin, R. R. Kerswell, and F. Waleffe, "Experimental observation of nonlinear travelling waves in turbulent pipe flow," Science **305,** 1594 (2004).

[23] A. T. Patera and S. A. Orszag, "Finite amplitude stability of axysimmetric pipe flow," J. Fluid Mech. **112,** 467–474 (1981).

[24] U. Brosa, "Turbulence without strange attractor," J. Stat. Phys. **55,** 1303–1312 (1989).

[25] S. J. Chapman, "Subcritical transition in channel flows," J. Fluid Mech. **451,** 35–97 (2002).

[26] L. N. Trefethen, S. J. Chapman, D. S. Henningson, A. Meseguer, T. Mullin, and F. T. M. Nieuwstadt, "Threshold amplitudes for transition to turbulence in a pipe," Technical Report No. 00/17, Oxford University Comp. Lab. (2000) .

[27] A. Meseguer and L. N. Trefethen, "A spectral Petrov-Galerkin formulation for pipe flow I: linear stability and transient growth," Technical Report No. 00/18, Oxford University Comp. Lab. (2000) .

[28] A. Meseguer and L. N. Trefethen, "A spectral Petrov-Galerkin formulation for pipe flow II: nonlinear transitional stages," Technical Report No. 01/19, Oxford University Comp. Lab. (2001) .

[29] F. Mellibovsky and A. Meseguer, "Global finite amplitude perturbations in medium aspect ratio pipe flow," J. Phys. Conf. Ser. **14,** 192–205 (2005).

[30] H. Schlichting, *Boundary-Layer Theory, McGraw-Hill Series in Mechanical Engineering* (McGraw-Hill, New York, 1968).

# List of figure captions

1. (a) Six-jet injection device used in Hof, Juel & Mullin experiments[1]. Fluid is injected from six azimuthally equispaced slits around a perimeter of the pipe at a fixed streamwise location. (b) Acceleration field $\partial_t \mathbf{u}$ at $t = 0$ and $z = 0$, resulting from the forcing $\mathbf{f}$ in (21). See the Appendix for details.

2. (a) Jet speed, $u_g$, measured at the point of maximum forcing norm as a function of time for different injection lapses $\Delta t_{\text{inj}} = 2, 3, 4, 5, 8$ and $16$ (solid curve ended with gray circles) with $\text{Re} = 4000$. The re-run for the same critical amplitude but with permanent forcing are represented to show the asymptotic behaviour of $u_g$ (dashed curves) and their saturation values $u^*$. (b) Normalized threshold amplitudes of Hof, Juel and Mullin[1] experiments (gray squares) and current computations (white circles) with $\text{Re} = 4000$.

3. Critical run at $\text{Re} = 4000$, with $\Delta t_{\text{inj}} = 20$. Each snapshot depicts azimuthal vorticity contours, $(\nabla \times \mathbf{u})_\theta$, of the perturbation field (basic flow removed) on top of a 3D view of a couple of axial vorticity iso-surfaces at $(\nabla \times \mathbf{u})_z = \pm 0.3$. The pictures correspond to $t = 20, 70, 130$ and $200$, and have been taken from a viewpoint travelling downstream at the same speed as the perturbation.

4. Growth of the turbulent patch as it is advected downstream. Black dots represent points fulfilling the criterion that $\langle u_z \rangle^2_{\text{rms}} \geq 0.5\%(U_{\text{cl}}/2)^2$. Dashed lines show the position of the trailing and leading edges as a function of time.

5. Experimental (gray squares) and computational (white circles) critical amplitude thresholds. Both sets of values have been normalized independently with respect to their critical amplitudes at $\text{Re} = 14000$.

6. Relative transient drop of $\text{Re}_a$ for slightly subcritical injections at different values of nominal Re, indicated next to each of the corresponding curves.

7. Cross-sectional cartesian coordinate system used in designing the jet corresponding to the first injection point.

## List of table captions

I. Computed threshold amplitudes $\mathcal{A}_{\text{num}}$, based on numerical measurement of $u^*$, for comparison with those corresponding to the experiments by Hof, Juel and Mullin[1], $\mathcal{A}_{\text{exp}}$. The quantities appearing in the last two rows are the normalized amplitudes according to equation (30).

impulsive
injection

$\varphi = \dfrac{\pi}{3}$

$\varphi$  $\varphi$

(a)

(2)  (1)

(3)  (0)

$\varphi$  $\varphi$  $g$

$\mathbf{f}_{\text{max}}$

(4)  (5)

(b)
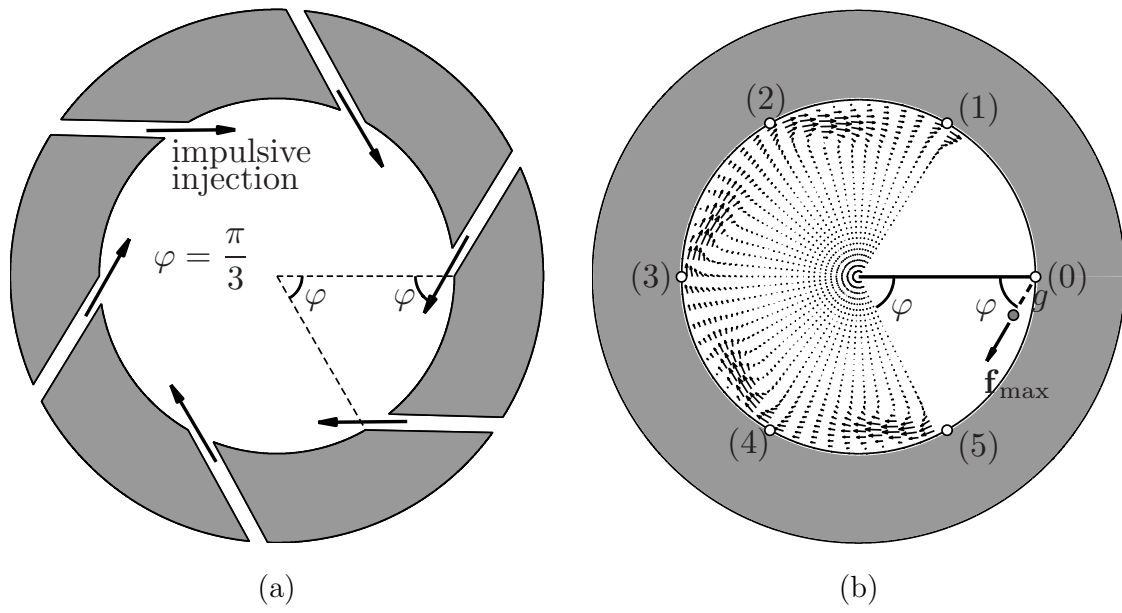
FIG. 1: Mellibovsky Phys. Fluids.

| $\Delta t_{\text{inj}}$ | $u^*$ | $\mathcal{A}_{\text{num}} \times 10^3$ | $\mathcal{A}_{\text{exp}} \times 10^3$ | $A_{\text{num}}$ | $A_{\text{exp}}$ |
|---|---|---|---|---|---|
| 4.0 | 0.157 | 1.495 | 6.167 | 1.48 | 1.72 |
| 8.0 | 0.112 | 1.280 | 4.443 | 1.26 | 1.24 |
| 10.0 | 0.100 | 1.225 | 4.244 | 1.21 | 1.19 |
| 14.0 | 0.090 | 1.167 | 4.045 | 1.15 | 1.13 |
| 16.0 | 0.081 | 1.106 | 3.834 | 1.09 | 1.07 |
| 24.0 | 0.068 | 1.013 | 3.581 | 1.00 | 1.00 |

TABLE I: Mellibovsky Phys. Fluids.

(a)

(b)

FIG. 2: Mellibovsky Phys. Fluids.

(a) $t = 20$

(b) $t = 70$

(c) $t = 130$

(d) $t = 200$

$0 \qquad z \qquad \Lambda/2 \qquad \Lambda$
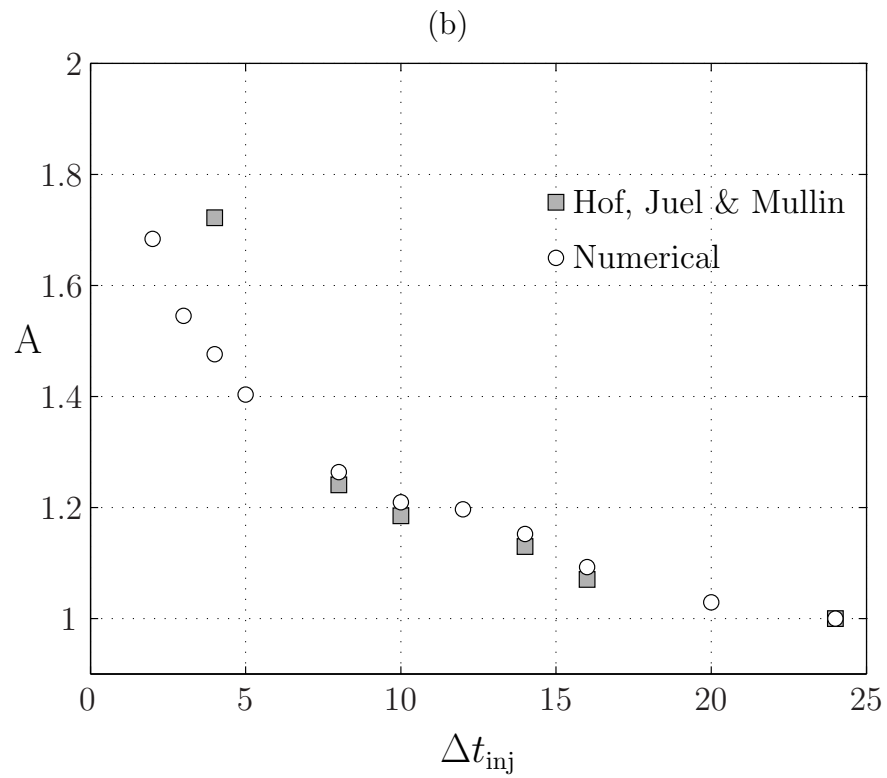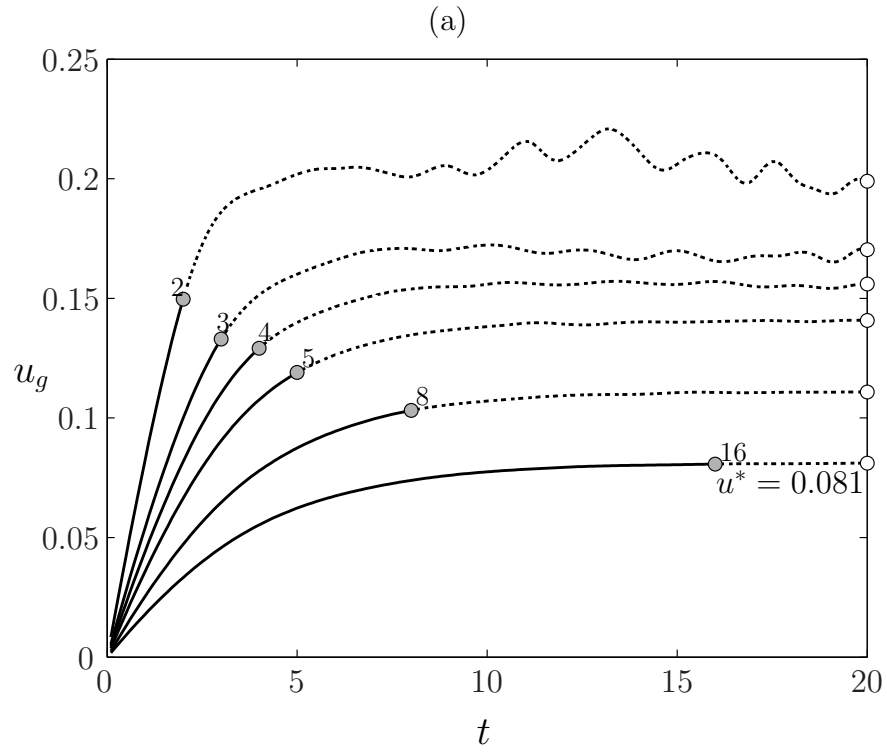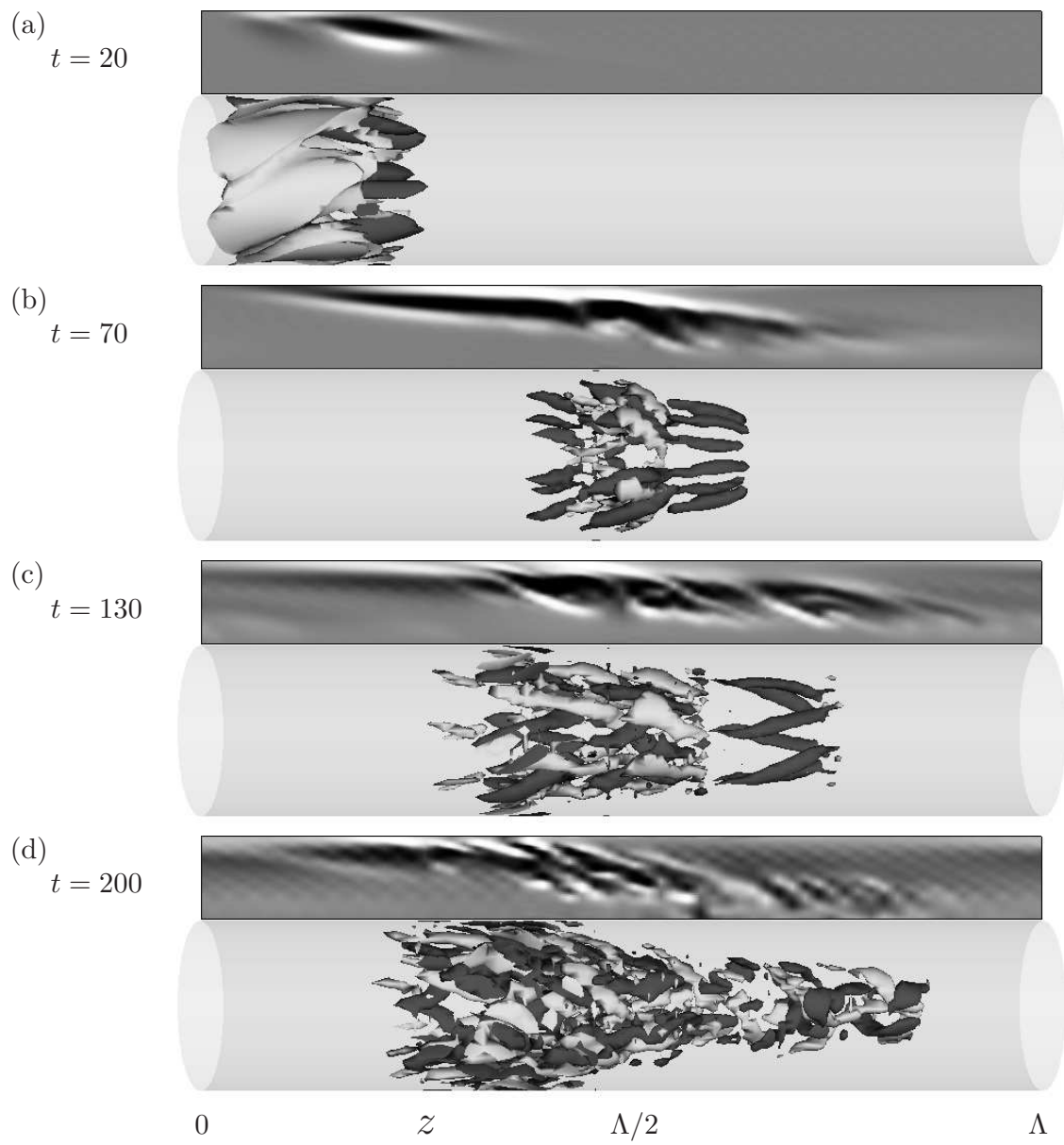
FIG. 3: Mellibovsky Phys. Fluids.
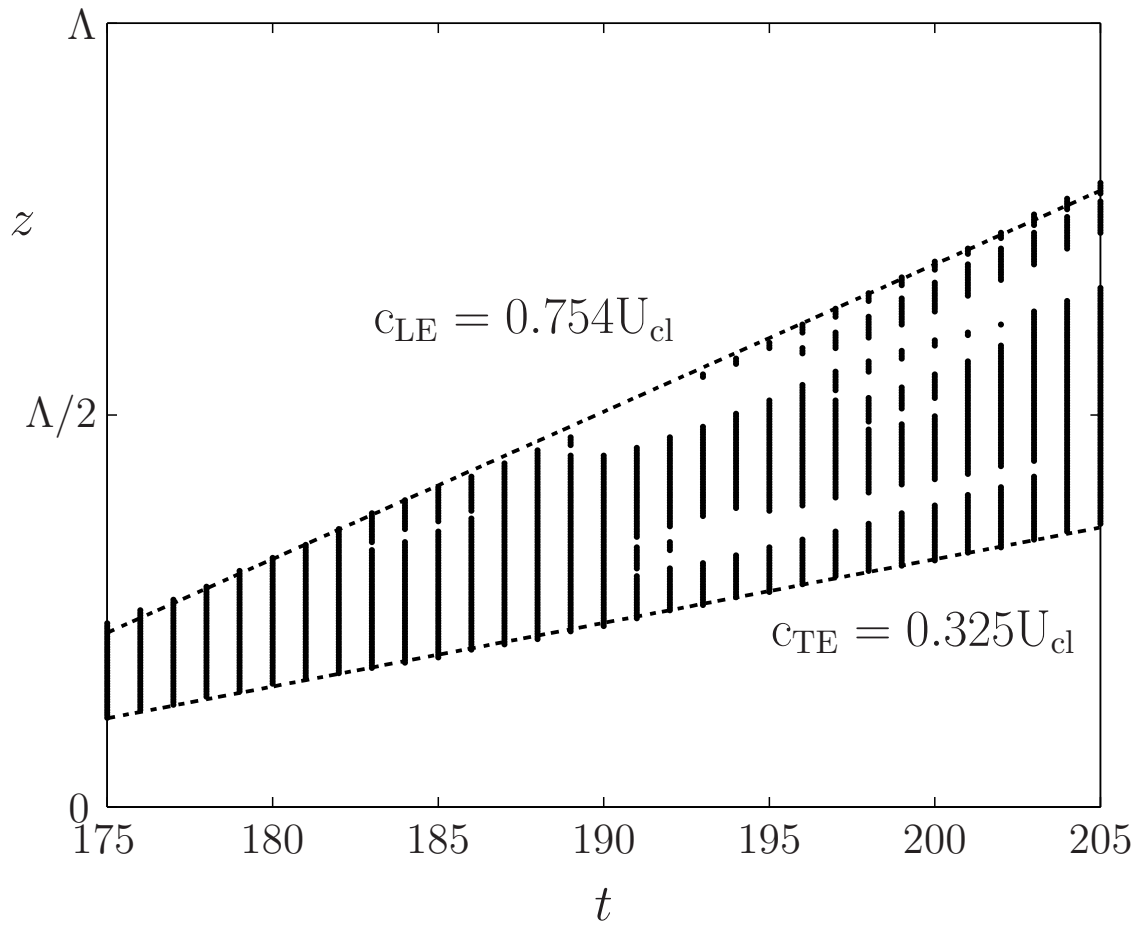
FIG. 4: Mellibovsky Phys. Fluids.
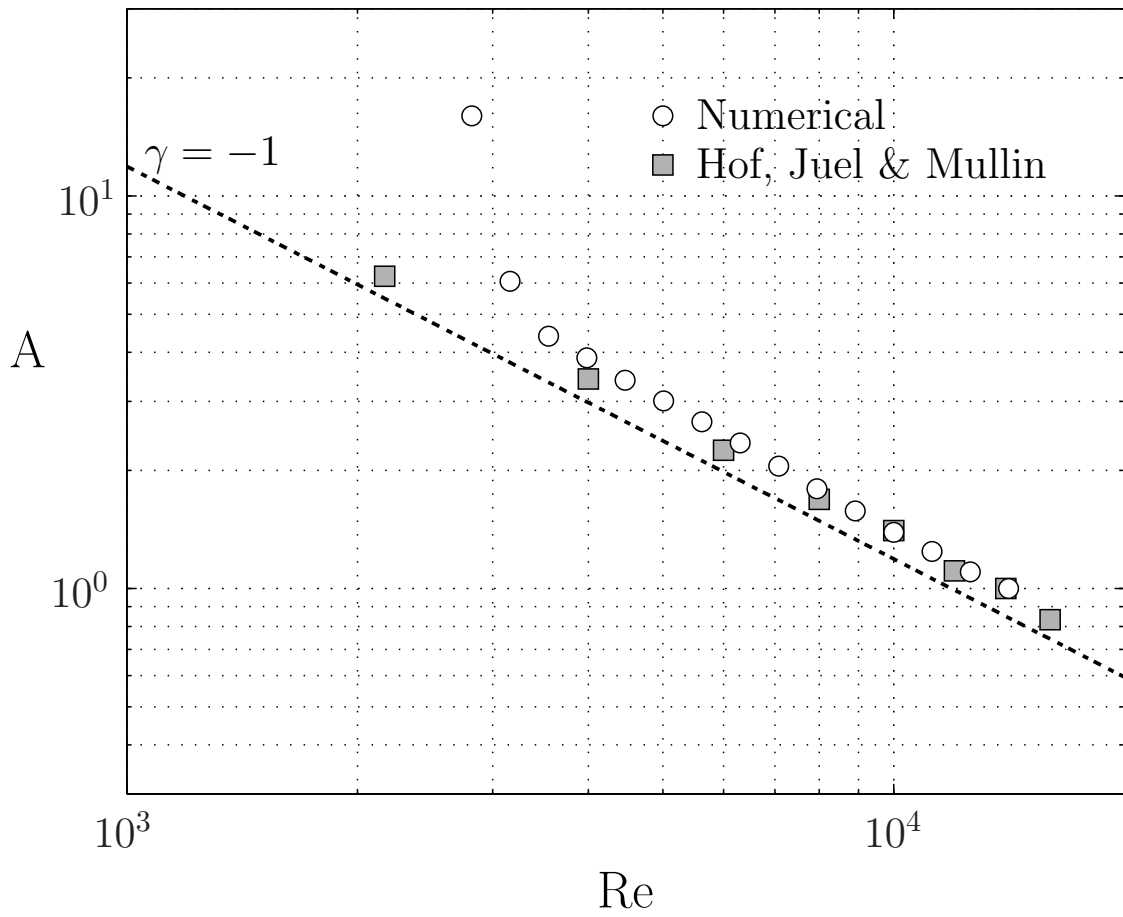
FIG. 5: Mellibovsky Phys. Fluids.
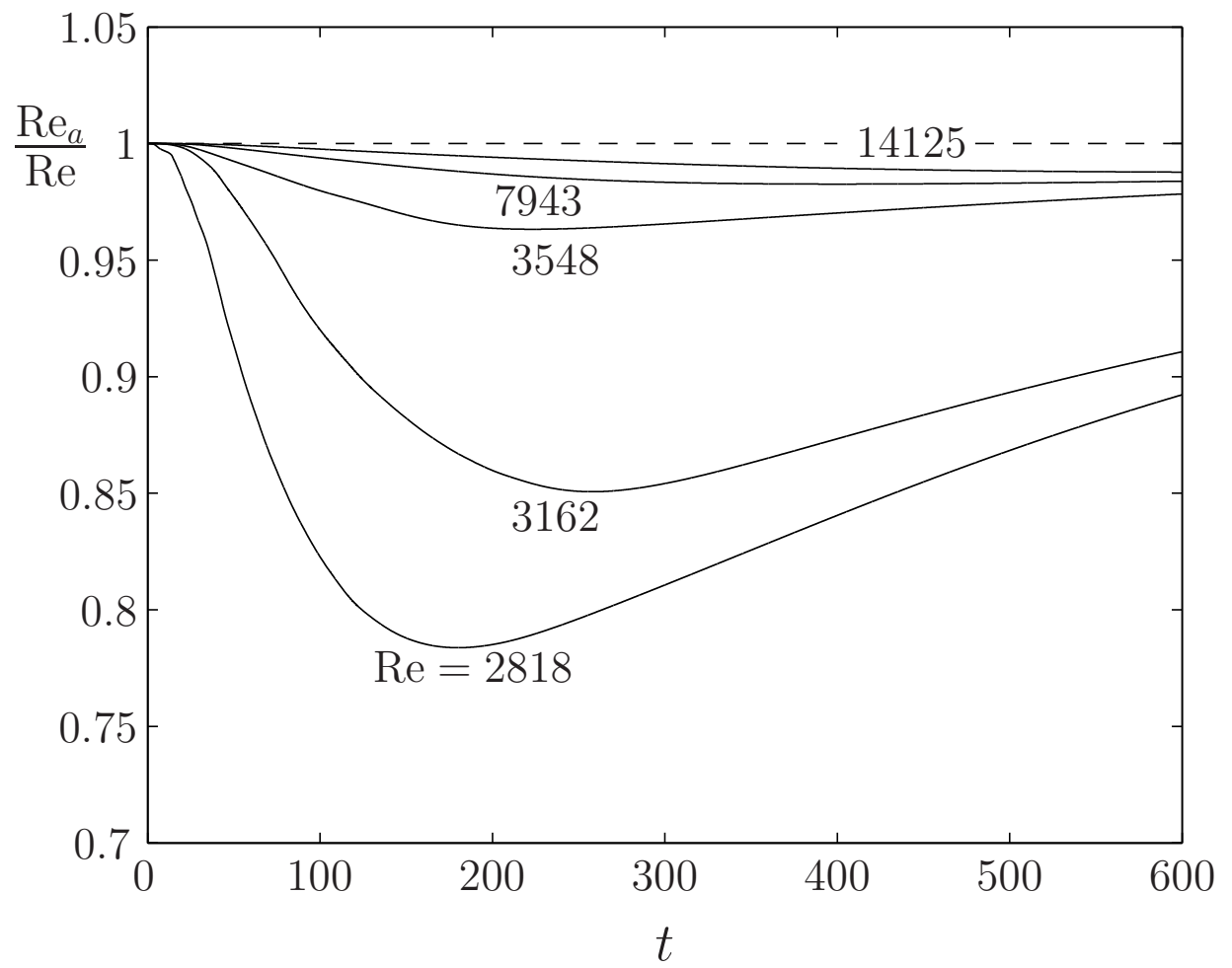
FIG. 6: Mellibovsky Phys. Fluids.

FIG. 7: Mellibovsky Phys. Fluids.